

**DESIGN, FABRICATION, AND CONTROL OF A
HIGH-ASPECT RATIO MICROACTUATOR FOR
VIBRATION SUPPRESSION IN A HARD DISK DRIVE**

**Kenn Oldham * Xinghui Huang * Alain Chahwan *
Roberto Horowitz **,¹**

** Computer Mechanics Laboratory, University of California at
Berkeley, 94720-1740 {oldham, xhhuang}@me.berkeley.edu*

*** Professor of Mechanical Engineering, University of
California at Berkeley, 94720-1740*

horowitz@me.berkeley.edu

Abstract: At bit densities now approaching 1 terabit per square inch, positioning the read-write head in a hard disk drive over data bits will require novel servo configurations and controllers. This paper presents a MEMS microactuator for installation in a dual-stage servo system for a hard disk drive and controller designs that utilize the microactuator to suppress vibration of the servo arm. The microactuator uses high-aspect ratio etching and deep trench isolation to generate high force densities and good mechanical robustness. The microactuator is installed in a hard disk drive and will be used to evaluate controllers designed to suppress airflow-induced vibration. Simulated and experimental results using PQ design methodology are presented.

Keywords: Microsystems, Disk memory, Multirate control, Actuators, Vibration

1. INTRODUCTION

As storage densities in hard disk drives increase, it becomes ever more difficult to position the read-write head over shrinking magnetic bits. Conventional disk drives position the read-write head using a single large voice-coil motor (VCM) that swings the read-write head across the disk on an arm and pivot consisting of a suspension and E-block (see figure 1). Unfortunately, airflow-induced vibration of suspension and E-block resonant modes disturbs this servo arm. At very high bit densities, approaching 1 terabit per square inch, this vibration is the dominant obstacle to accurate positioning of the read-write head. A proposed solution to this problem is to include a second-stage actuator in the servo system. Three types of dual-stage actuation have been proposed. The first is built

into the suspension and moves the lower portion of the slider and read-write head, typically using piezoelectric materials (Evans *et al.*, 1999) (I. Naniwa and Sato, 1999) This “actuated suspension” approach is the simplest to implement, but still faces problems of structural vibration. The second approach inserts a MEMS microactuator between the suspension and slider. This “actuated slider” method places the actuator beyond the region of structural vibration, but requires a more complicated process flow and high actuation voltages. Electrostatic (Horsley *et al.*, 1999) (White *et al.*, 2004), piezoelectric (Soeno *et al.*, 1999) (Kuwajima and Matsuoka, 2002), and electromagnetic (Tang *et al.*, 1996) actuation forces have been proposed for this configuration. The final approach places the second stage actuator in the slider itself at the read-write head (Nakamura *et al.*, 1998) (Kim and Chun, 2001). This “actuated head” arrangement gives

¹ Partially supported by Berkeley Computer Mechanics Laboratory and Information Storage Industry Consortium

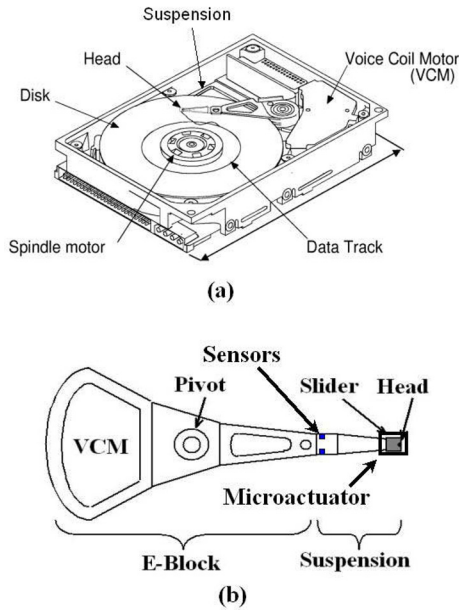


Fig. 1. Components of (a) conventional disk drive (b) dual-stage instrumented servo assembly

ideal actuation location, but the integration of head, slider, and actuator fabrication is very difficult.

Servo system performance can also benefit from dedicated vibration sensing, in the form of an instrumented suspension. Such a suspension incorporates strain sensors on the suspension (see Figure 1b). These can detect vibration at higher sampling rates than may be obtained from a drive's position error signal. Optimization and fabrication of such suspensions are described in (Oldham *et al.*, 2004).

This paper focuses on an actuated-slider microactuator (hereafter referred to as the MA) and the control schemes that utilize it. The MA demonstrates advantages to force generation and mechanical properties from high-aspect ratio deep trench etching. As part of an experimental testbed for dual-stage servo control, it is compatible with a MEMS-ready prototype suspension and addresses issues often neglected by other proposed actuated slider designs, such as formation of metal interconnects, robust structure for installation, and dedicated capacitance sensors for relative position error sensing.

The MA that is discussed in this paper was designed and fabricated by our research group for installation in an instrumented suspension, in order to test a variety of track-following and vibration suppression multirate control schemes. Experimental results presented in this paper are in close agreement with simulation results and verify system modeling and control methodology assumptions.

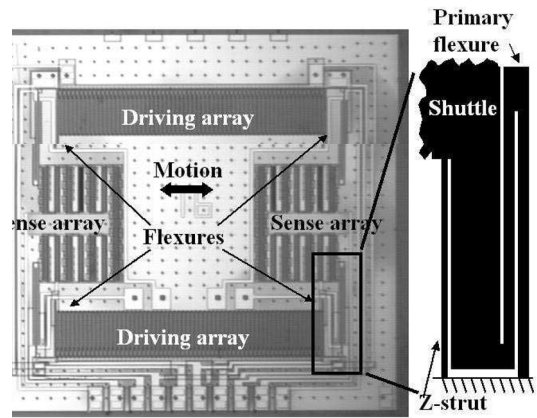


Fig. 2. Completed microactuator, flexure design inset

2. HIGH-ASPECT RATIO MICROACTUATOR

2.1 Microactuator design

This section describes special features of the MEMS MA, especially those derived from the ability to form very high-aspect ratio structures using deep reactive-ion etching (DRIE). The MA is arranged with a central shuttle for the slider and read-write head, which is connected at each corner by a flexure to a fixed base, as shown in Figure 2. Electrostatic driving and sensing capacitive finger arrays surround the moving shuttle.

High-aspect ratios in actuation The MA is driven by electrostatic gap-closing parallel-plate arrays. In parallel plate arrays, force generation is inversely proportional to the squared gap between plates, giving large forces when finger length and thickness are much larger than gap width. With DRIE, the ratio of thickness to gap width may reach 20:1, producing large forces at relatively low voltages.

Deep trench isolation DRIE trenches refilled with insulating material may be used to counteract the fact that electrostatic driving forces are always attractive. Two arrays are generally desired to drive a MA in either direction and to linearize the dependence of force on driving voltage. Typically, opposing parallel-plates arrays must be physically separated, requiring a large amount of space, as shown in Fig. 3b. Deep trench isolation allows the differential fingers to be physically connected but electrically isolated, as shown in Fig. 3a, increasing the number of plates that can be used for actuation.

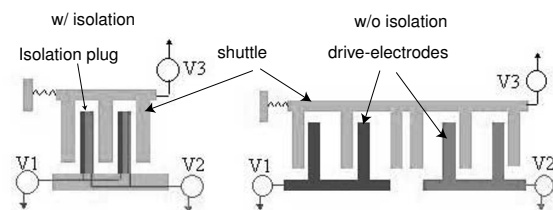


Fig. 3. Parallel plates (a) with or (b) without deep trench isolation

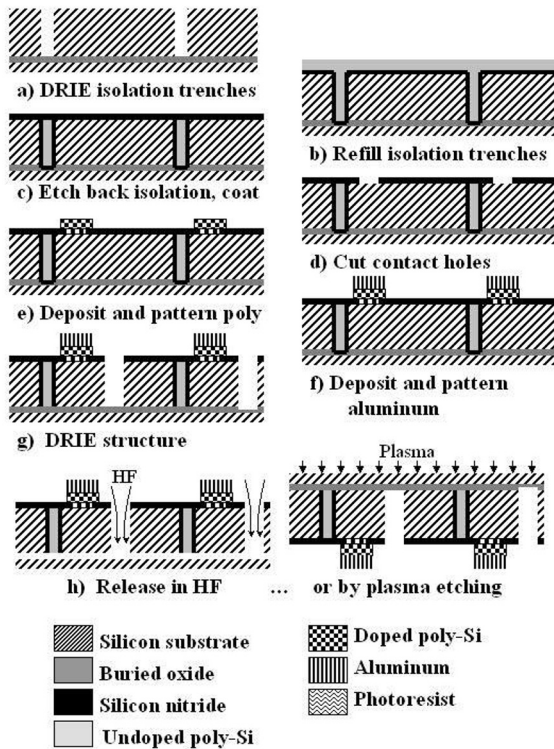


Fig. 4. Microactuator fabrication process

Deep trench isolation also simplifies the electrical operation of the device. Isolated portions of the substrates may be used to cross signals underneath surface level interconnects, so that the entire device requires only one metallization layer. Isolated plugs may also act as stoppers to prevent the MA shuttle from shorting to stator fingers, due to an external shock or electrostatic pull-in.

Flexure design The MA also exhibits a novel compound flexure design. It is important that the MA be very compliant in the direction of desired motion but very stiff in all other directions. The least stiff secondary direction is directly out-of-plane, for which relative stiffness is controlled by the ratio of device thickness to spring width. Unfortunately, interconnects to the read-write head limit the minimum width of the primary flexures. Therefore, thin secondary struts are added to increase the out-of-plane structural stiffness, as shown in the inset of Fig. 2, with negligible effect on in-plane compliancy.

Relative position sensing The MA includes a capacitive sensing array for measuring the position of the shuttle relative to the MA base. The benefits of using this signal in control design were suggested in (Li and Horowitz, 2001).

2.2 Microactuator fabrication

MAs were built from silicon-on-insulator (SOI) wafers with a 100 μm device layer (refer to Fig. 4). Fabrication began by forming the deep trench isolation plugs

(a). Trenches were etched via DRIE, coated with silicon nitride, and refilled with undoped polysilicon (b). Silicon nitride provides good electrical isolation, but has high residual stress and is not sufficiently conformal. The undoped polysilicon refills the deep trenches more evenly. Polysilicon on the surface of the substrate was etched back to the nitride film by reactive-ion etching. The entire wafer is then coated by a second silicon nitride film (c). Contact holes through the nitride layer are etched by reactive-ion etching (d). Next, highly doped polysilicon is deposited and patterned as interconnects, to provide a robust and adhesive base layer for metal (e). An aluminum layer is evaporated onto the substrate and patterned identically to the polysilicon (f). The silicon/aluminum stack has both high conductivity and robustness to potential damage during release of the devices. Lastly, DRIE defines the geometry of the device (g).

MAs may be released from the substrate by either of two methods, as shown in Figure 4h. The simpler method is to immerse dies in hydrofluoric acid (HF) until individual MAs may be removed from the substrate. This is a reliable, high yield procedure, but it removes any aluminum on the device, leaving only doped polysilicon interconnects and reducing the quality of any signal from the capacitive sensing array. Alternatively, etching through the SOI handle layer from the backside of the device preserves aluminum lines, at the cost of added processing steps. Backside coatings are removed and dies are bonded with photoresist face down on an encapsulated handle wafer. The dies are blanket plasma etched back to the buried oxide. Then, drops of HF etch the buried oxide and oxygen plasma scours and/or heated photoresist stripper remove photoresist residue from the MAs.

2.3 Microactuator Performance

MAs with varying spring widths were produced by both release techniques. The dynamic response of two such MAs after slider installation is shown in Fig. 5, measured by a Laser Doppler Velocimeter (LDV). The responses show single resonant modes between 1.7 and 2.2 kHz, with clean responses to better than 20 kHz, allowing effective control of suspension vibration modes expected to appear above 4 kHz. The MA resonant modes observed in Fig. 5 are highly damping for a MEMS device, due to large amounts of squeeze-film damping that takes place between the MA's parallel plate arrays; this damping is also advantageous for control.

Force densities extracted from the LDV measurements indicate that the MAs generate forces as large or larger than previously published results from MAs for hard disk drives. Even beyond 10 kHz, the MA is capable of producing over 1 nm displacement per volt. However, the forces are only about 15% of theoretical predictions. Table 1 lists extracted MA properties for one

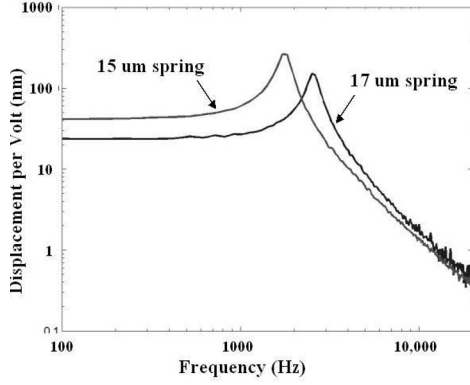


Fig. 5. Stand-alone microactuator dynamic response

Table 1. Measured microactuator performance compared to predictions, before and after sidewall erosion, 15 V bias

Parameter	Units	Predicted value	Prediction after erosion	Measured value
Spring width	μm	17	15.7	15.7
Natural Frequency	Hz	2390	2470	2517
Force per Volt	$\frac{\mu\text{N}}{\text{V}}$	77	18	13
Motion per Volt, static	$\frac{\mu\text{m}}{\text{V}}$	157	34	24
Motion per Volt, 10 kHz	$\frac{\mu\text{m}}{\text{V}}$	9.5	2.4	1.4
Damping Ratio		N/A	N/A	8 %

MA, with 17 μm springs. The discrepancy is mostly due to sidewall erosion of the DRIE trenches. Scanning electron microscope images showed trenches to be 0.5 to 1.5 μm wider than anticipated. Other factors include simplifications in our analytical spring model and imperfect installation of the slider and interconnects.

MAs have been successfully installed and flown over a spin stand at disk speeds up to 10,000 rpm. Electrical connections from suspension to metallized MAs are performed by ultrasonic wire bonding. A sample MA with 17 μm wide main spring was installed in a 3.5 inch, 7200 rpm disk drive for in-drive testing and controller evaluation.

3. DUAL-STAGE MODEL WITH INSTRUMENTED SUSPENSION

This section introduces the model of the dual-stage actuation scheme. Fig. 6 shows the block diagram of the dual-stage actuator with an instrumented suspension, and Fig. 8 shows its experimental frequency response and fitted model. In these figures, u_v and u_m are the control inputs to the VCM and MA respectively, y_v is the displacement of the suspension tip, also referred to as position error signal, PES, y_p is the strain sensor output from the instrumented suspension, y_m is the motion output of the slider/head relative to the sus-

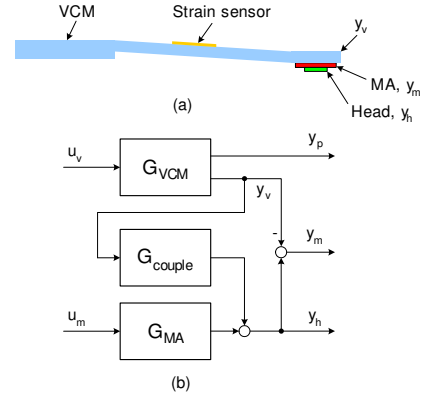


Fig. 6. Block diagram of the dual-stage actuator

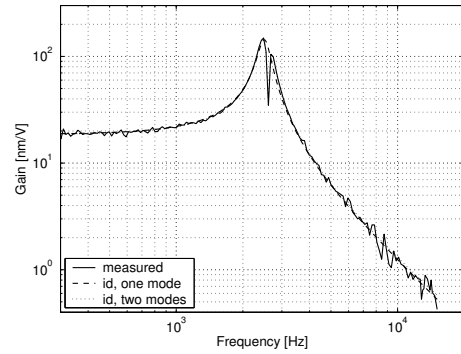


Fig. 7. In-drive frequency response of microactuator

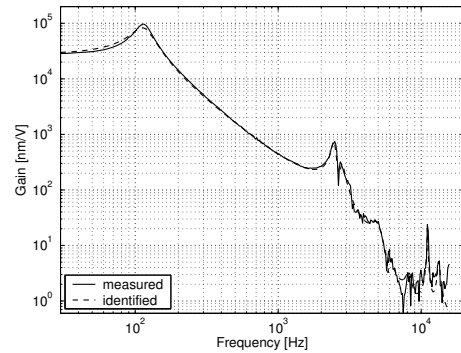


Fig. 8. Frequency response of the VCM-suspension assembly

pension tip, and y_h is the absolute head displacement, as measured by the disk's position error signal.

The transfer function of the suspension, G_{VCM} , can be expressed as

$$G_{\text{VCM}} = k \sum_{i=1}^7 \frac{r_i}{s^2 + 2\zeta_i \omega_i s + \omega_i^2}, \quad (1)$$

where the loop gain k is a lumped gain from the current amplifier, D/A converter and position sensing, and ω_i , ζ_i and r_i are the natural frequency, damping ratio and modal constant of mode i , respectively. The first mode results from the flex cable and bearing friction. The remaining modes are VCM, e-block, and suspension vibration modes. Two major modes, located at 5 kHz and 11 kHz, are considered in controller design.

The full 14 order model is used for performance analysis of the closed-loop system.

The MA can be modeled as a single mass-spring-damper system with a resonance mode around 2.5 kHz. Its transfer function is

$$G_{\text{MA}}(s) = \frac{A_m}{s^2 + 2\zeta_m\omega_m s + \omega_m^2}, \quad (2)$$

and its experimental and modeled frequency responses are also shown in Fig. 7. The parameters for G_{MA} are $A_m = 4.6$ m/V, $\zeta_m = 0.068$, and $\omega_m = 2.51$ kHz. Dynamics of the MA after installation closely match the stand-alone response of the MA, except for a bifurcation of the resonant mode just above the expected resonant frequency; this is likely a result of minor damage during installation. It is not included in the model, but may affect system performance. Capacitive sensors were incorporated into the MA structure so that the relative position error signal, or RPES, $y_m = y_h - y_v$, is measurable, though the required sensing circuit was unfinished at the time of writing.

VCM actuation can excite the MA dynamics through the suspension tip, since the MA is translational. However, it can be reasonably assumed that the MA actuation will not excite the suspension dynamics due to its small moving inertia, and this is confirmed experimentally, as shown in Fig. 7. The coupling dynamics from the suspension tip displacement, y_v , to the slider motion output, y_h , can be expressed as

$$G_{\text{couple}}(s) = \frac{2\zeta_m\omega_m s + \omega_m^2}{s^2 + 2\zeta_m\omega_m s + \omega_m^2}. \quad (3)$$

4. CONTROL DESIGN

4.1 MA Damping

When the RPES output, y_m , of the MA is available, active damping can be applied to the MA to obtain a well-behaved system and simplify the following controller design, as described in (Li and Horowitz, 2001) and (White and Hirano, 2003). The plant is first discretized at 50 kHz with a zero-order hold. Applying pole placement using a Diophantine equation, the damped MA dynamics can be set to a closed-loop polynomial chosen by the designer, usually with unity damping ratio.

4.2 Vibration Damping and Compensation

With the damped MA, a suspension vibration damping and compensation controller K_{in} is designed using y_p . The design of K_{in} is formulated as a standard LQG problem minimizing the following cost function

$$J = E \{ y_h^2(k) + R u^2(k) \}. \quad (4)$$

The resulting control effect on the VCM is to actively damp off-track resonance modes, while the effect on

the MA is to provide additional motion to compensate for airflow-excited vibrations at the read/write head. Simulation results in Fig. 9 show the control effect when both the MA damping and the vibration controller are closed around the plant, creating a double-input single-output (DISO) system.

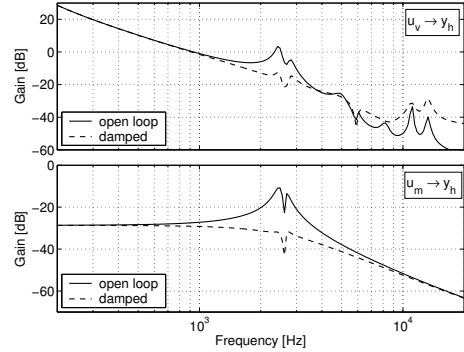


Fig. 9. Plant dynamics with/without vibration damping and compensation.

4.3 Track-following Control

Whether or not an instrumented suspension and RPES is available for damping the plant, a low-rate track-following controller can be designed for the DISO system using a straightforward design method called the PQ method. This method reduces a control design problem for DISO systems to two standard control design problems for SISO systems. The first part of the PQ method directly addresses the issue of actuator interference as a function of frequency, and the second part allows the use of traditional loop shaping techniques to achieve the desired system performance. The reader is referred to (Schroek and Messner, 1999) for more details of this method.

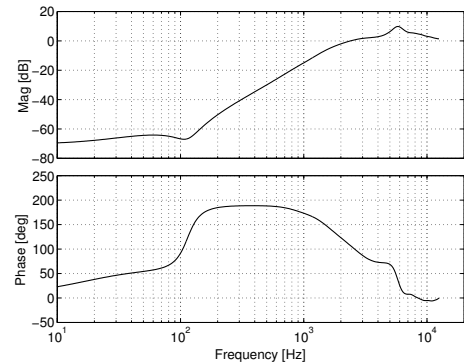


Fig. 10. Closed-loop sensitivity responses of the fully instrumented dual-stage system (simulation)

Simulation results in Fig. 10 show the closed-loop sensitivity of the dual-stage system based on the identified model when both RPES and instrumented suspension are available. The closed-loop servo bandwidth is about 2.1 kHz, with enough low-frequency error rejection and a mild peak of 7.2 dB. The projected rms tracking error of such a system is 4.8 nm.

5. EXPERIMENTAL RESULTS

At this time, only the PES is available on the dual-stage system, so the controller used for experimental verification is less aggressive than the controller incorporating inner loop damping in the previous section. Without inner loop damping control of the suspension and MA, the PQ method can still be applied to design a track-following controller, but the servo bandwidth is only 650 Hz. Nevertheless, experimental measurements of the closed loop system verify operation of the current dual-stage setup and accuracy of the system model. Fig. 11 shows agreement between the predicted and experimental sensitivity function, except near the flex cable vibration mode. Fig. 12 shows the significant closed-loop improvement of the PES power spectrum at low frequencies. Total rms tracking error of the system is reduced from 764 nm in the open-loop system to 10.8 nm in the closed-loop system.

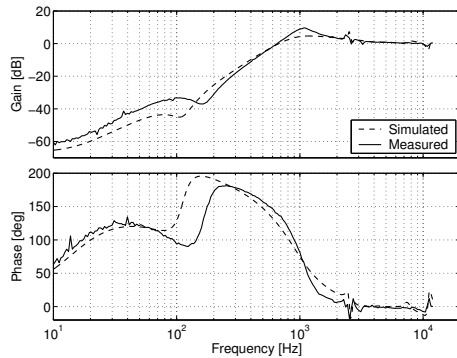


Fig. 11. Closed-loop sensitivity responses of the dual-stage system (experimental)

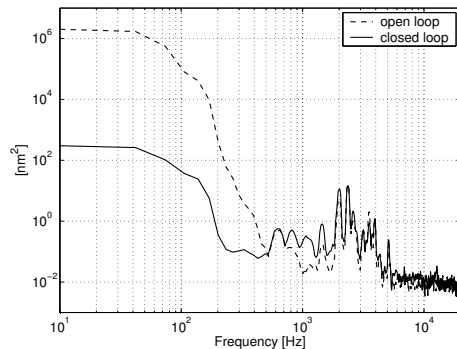


Fig. 12. Power spectrum of the PES

6. CONCLUSION

A robust, high force microactuator has been fabricated and used to suppress vibration in a dual-stage control scheme for hard disk drives. The microactuator utilizes high-aspect ratio trenches and deep trench isolation to form a compact electrostatic parallel-plate array. This produces very large electrostatic forces, though performance was limited by imperfect processing of the deep trenches. The microactuator demonstrates a very clean dynamic response, with especially

good gains at high frequencies. Multi-rate controllers are presented to capitalize on the microactuator presence. Closed-loop dual-stage servo control is verified experimentally, while additional sensors are under development to take full advantage of dual-stage capabilities. Using PQ controllers, the current assembly has achieved 10.8 nm rms tracking error, while a system with all desired sensor signals is projected to 4.8 nm rms error.

REFERENCES

- Evans, R.B., J.S. Griesbach and W.C. Messner (1999). Piezoelectric microactuator for dual-stage control. *IEEE Trans. on Magn.* **35**, 977–81.
- Horsley, D., N. Wongkommet, R. Horowitz and A. Pisano (1999). Precision positioning using a microfabricated electrostatic actuator. *IEEE Transactions on Magnetics* **35**, 993–999.
- I. Naniwa, S. Nakamura, S. Saegusa and K. Sato (1999). Low voltage driven piggy-back actuator of hard disk drives. *IEEE International MEMS 99 Conference* pp. 49–52.
- Kim, B.-H. and K. Chun (2001). Fabrication of an electrostatic track-following micro actuator for hard disk drives using soi wafer. *Journal of Micromechanics and Microengineering*.
- Kuwajima, H. and K. Matsuoka (2002). Thin film piezoelectric dual-stage actuator for hdd. *Inter-Mag Europe, Session BS04* pp. 229–236.
- Li, Y. and R. Horowitz (2001). Mechatronics of electrostatic microactuators for computer disk drive dual-stage servo systems. *IEEE/ASME Trans. Mechatronics* **6**(2), 111–121.
- Nakamura, S., K. Suzuki, M. Ataka and H. Fujita (1998). An electrostatic microactuator for a magnetic head tracking system of hard disk drives. *Advances in Info. Storage Systems* **10**, 83–99.
- Oldham, K., S. Kon and R. Horowitz (2004). Fabrication and optimal strain sensor placement in an instrumented disk drive suspension for vibration suppression. *Proc. Amer. Control Conf.*
- Schroek, S.J. and W.C. Messner (1999). On controller design for linear time-invariant dual-input single-output systems. *Proc. Amer. Control Conf.* pp. 4122–4126.
- Soeno, Y., S. Ichikawa, T. Tsuna, Y. Sato and I. Sato (1999). Piezoelectric piggy-back microactuator for hdd. *IEEE Trans. Mag.* **35**(2), 983–987.
- Tang, W., V. Temesvary, J.J. Yao, Y.-C. Tai and D.K. Miu (1996). Silicon microactuators for computer disk drives. *Japaneses J. Appl. Physics*.
- White, M., T. Hirano, H. Yang, K. Scott, S. Pattnaik and F.-Y. Huang (2004). High bandwidth hard disk drive tracking using a moving-slider mems microactuator. *8th IEEE Int'l Workshop Advanced Motion Control* pp. 299–304.
- White, M.T. and T. Hirano (2003). Use of relative position signal for microactuators in hard disk drives. *Proc. Amer. Control Conf.* **3**, 2535–2540.